E-Band Wide-Angle Scanning Antenna Array Using Controllable Decoupling Paths With High Isolation and Good Active Impedance Matching

Wanchen Yang, *Senior Member, IEEE*, Zhixin Liang, Xiangchuan Wang, *Member, IEEE*, Xufu Liu, Wenjie Feng, *Senior Member, IEEE*, Wenquan Che, *Fellow, IEEE*, and Shilong Pan, *Fellow, IEEE*

***Abstract*—This article presents a E-band phased antenna array based on controllable decoupling path for wide-angle scanning applications. The decoupling path is implemented by loading a pair of I-shaped strip with two grounded vias and a parasitic grounded via on both sides of the antenna to eliminate the inherent coupling between elements in array, enabling the control of amplitude and phase. According to the equivalent circuit analysis, the I-shaped strip is mainly used to control the phase and magnitude of the energy in the decoupling path, and the parasitic via is used to further adjust the phase of the energy, accurately canceling the inherent coupling between different elements of the array. To verify this, a wide-scanning phased array using stacked metasurfaces was designed, where the controllable decoupling paths are symmetrically located on both sides of the elements along the E-plane, achieving high isolation and minimal impact on impedance matching. As a result, the array has a high isolation of over 20 dB and a wide-angle beam scanning of up to ±62° within a broad bandwidth of 66–76 GHz (19.7%). Additionally, the gain fluctuation is less than 2.9 dBi, the active S-parameters remain below −10 dB, and the antenna efficiency reaches 71%. Compared with other works, this array has the advantages of wide-angle scanning, high isolation, and good active impedance matching in the E-band and has potential application prospects in future millimeter-wave (mm-Wave) communications.**

***Index Terms*—Decoupling path, high isolation, stacked metasurface, wide-angle scanning.**

I. Introduction

RECENTLY, with the rapid development of wireless communication technology, millimeter-wave (mm-Wave) has been applied in military, civil, and industrial sectors [1], [2]. A wide range of azimuth and pitch beam scanning can be achieved in millimeter-wave (mm-Wave) frequency band by using phased array technology. Therefore, improving the scanning performance of arrays has become the focus of current research. The scanning performance of the array can be improved by reducing the distance between elements, broadening antenna beams, and reconfigurable radiation modes. Currently, radiation-mode reconfigurable antennas [3], meta-lenses antenna [7], [8], metasurface structures [9], antenna beamwidth [12], [13], [14], [15], and tightly coupled arrays [16], [17], [18] have been extensively studied. In [16], a compact patch antenna array with two decoupling structures exhibits a low isolation of only 13 dB. It is well-known that poor isolation can lead to high active S-parameters, reduced radiation efficiency, and rapid loss during scanning.

Currently, two methods have been studied for enhancing isolation. One is to block the coupling path. In large-scale arrays, structures, such as electrical tape gap electrical bandgap (EBG) and perfect electrical conductor (PEC) perfect magnetic conductor (PMC) walls [18], [19], [20], are commonly employed to resist inherently coupled paths. The compact wide-beam mm-Wave 45° polarization low-temperature co-fired ceramic (LTCC) phased array proposed in [21] achieves a scanning angle of ±58° and a high isolation of 21 dB within the frequency range of 19.6%. However, the scanning range of the array in this study is smaller than that proposed in this article. The second method is to offset the inherent coupling path by introducing additional paths. It requires that the equal amplitude and inverse phase of the two paths are satisfied within the working band. In the two-elements array or small-scale arrays, neutralization line and decoupling networks [22] are commonly utilized, but the additional impedance matching networks of these two methods will increase the design complexity of large-scale arrays. Consequently, the antenna array decoupling surfaces and band-based stubs are proposed in [22], [23], [24], [25], [26], and [27]. In [28], a novel planar decoupling technique is employed to achieve a high isolation of 22 dB and a scanning range of ±60° over a relative bandwidth of 16.7%. However, the radiation efficiency is significantly reduced by gain drop during array scanning.

Inspired by the above works, a controllable decoupling path is proposed and implemented for wide-angle scanning in (mm-Wave) phased arrays. The concept of constant amplitude and reverse phase cancellation is employed by this article to achieve isolation performance exceeding 20 dB and active S-parameters less than −10 dB. Moreover, validation with 1 × 2 and 1 × 4 arrays shows that this method can be

Received 11 August 2025; revised 29 October 2025; accepted 3 November 2025. Date of publication 8 December 2025; date of current version 13 February 2026. This work was supported in part by the National Natural Science Foundation of China under Grant 62471219, Grant 62321002, and Grant 62231014; and in part by the Fundamental Research Funds for the Central Universities under Grant NE2025004. *(Corresponding author: Wanchen Yang.)*

Wanchen Yang, Zhixin Liang, Xiangchuan Wang, and Shilong Pan are with the College of Electronic and Information Engineering, Nanjing University of Aeronautics and Astronautics, Nanjing 211106, China (e-mail: wcyang@nuaa.edu.cn).

Xufu Liu, Wenjie Feng, and Wenquan Che are with Guangdong Key Laboratory of Millimeter-Waves and Terahertz and the School of Electronic and Information Engineering, South China University of Technology, Guangzhou 510641, China.

Digital Object Identifier 10.1109/TAP.2025.3638438

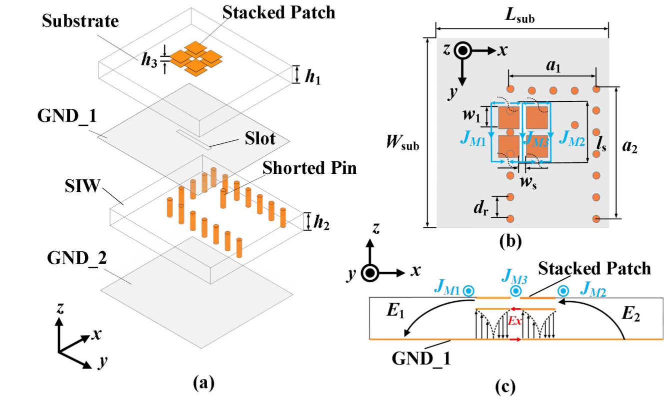

Fig. 1. Topology and the electric field distribution of the stacked metasurface element. (a) Three-dimensional view, (b) top view, and (c) side view of electric field E and magnetic current JM distribution in antiphase TM20 mode (parameters: w_1 = 0.3 mm, d_r = 0.3 mm, a_1 = 1.2, a_2 = 1.8 mm, h_1 = 0.376 mm, h_2 = 0.282 mm, W_{sub} = 2.61 mm, L_{sub} = 2.3 mm, l_s = 0.85 mm, and w_s = 0.1 mm).

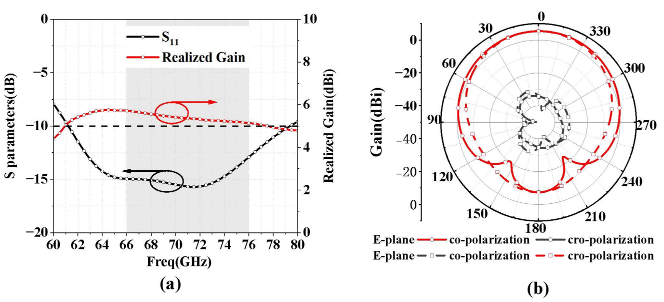

Fig. 2. Performance of the antenna element. (a) S-parameters and realized gain and (b) radiation pattern.

extended to large-scale arrays. After this, the EBG structures are integrated on both sides of the array. A ±62° beam scanning is achieved in the working band with a gain drop of less than 2.9 dBi. Therefore, the proposed method ensures favorable S-parameters and wide-angle scanning performance for the 4 × 4 phased arrays integrated into the package using the LTCCs process.

II. High-Isolation Wide-Angle Scanning Antenna Array With Good Active Impedance Matching

This section presents the development of a wide-angle scanning phased array with high isolation and good active impedance matching. The design follows a path from the individual antenna element to the 4 × 4 phased arrays system and is elaborated in Sections II-A–II-C.

A. Wideband Stacked Metasurface-Based Antenna Element

As we know, metasurface antennas with TM resonant modes as the traditional patch antenna have been widely used due to their advantages of simple structure, compactness, and easy integration. To address the coupling issue between (mm-Wave) arrays and the performance limitations of wide-angle scanning, a new wideband wide-beam antenna utilizing stacked miniaturized metasurface is presented in Fig. 1. The electric field distribution of the antiphase TM_{20} mode of the antenna is illustrated in Fig. 1(c). When the metasurface is excited, the horizontal electric field E_x would be generated and two electric fields E_1 and E_2 are produced on the radiation edge. Meanwhile, the magnetic currents J_{M1}, J_{M2}, and J_{M3} in the same direction are also excited by the three slots to generate an axial radiation pattern, resulting in a wideband and low profile. The miniaturization and wide beam performance are achieved by the incorporation of interlayer capacitances in the stacked design, while broadband impedance matching is fulfilled using short pins. In Fig. 2(a), the relative bandwidth of the antenna element at −10 dB is approximately 25.6% (61.2–79.4 GHz) with a gain drop of less than 0.5 dBi. Fig. 2(b) shows that the E-plane features a 3-dB beamwidth of up to 120°, while maintaining a cross-polarization level below 35 dB.

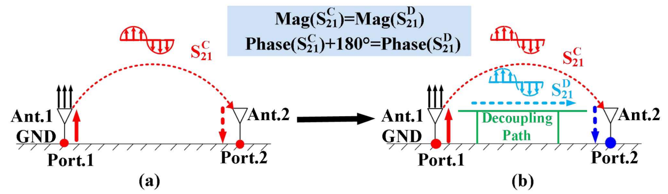

Fig. 3. Principle of controllable decoupling path for two elements. (a) Without decoupling path and (b) with decoupling path.

B. Analysis and Design of Controllable Decoupling Path of Linear Array

The size of the antenna element effectively reduced to only 0.16 λ_0 by using the stacked metasurface, but inherent coupling between the elements is still existing. In order to solve this problem, a controllable decoupling path is proposed. The effectiveness of the decoupling path is validated through equivalent circuit analysis and subsequently implemented in a 4 × 4 array configuration.

The inherent coupling between the two elements includes space coupling caused by EM wave propagation and ground coupling resulting from surface wave and the feeding network. In order to visually illustrate the operation of controllable decoupling paths, the conceptual model shown in Fig. 3 is used to simulate the cancellation process of inherently coupling and decoupling paths in a 1 × 2 array. When port 1 is excited, most of the energy radiates into space, and a part of energy is coupled into port 2, which is called the inherent coupling S_{21}^C. Then, a new energy in a decoupling path S_{21}^D is introduced to satisfy that the equal amplitude and inverse phase with S_{21}^C, so as to effectively offset the inherent coupling. The subarray structure of the 1 × 2 stacked metasurface antenna, as depicted in Fig. 4, consists of two identical stacked metasurface antenna elements distributed along the x-axis with an interelement spacing of $0.38\lambda_0$. The controllable decoupling path is symmetrically loaded between the two elements.

To obtain a controllable decoupling path, the equivalent circuit model and HFSS simulation model were established, as shown in Fig. 5(a) and (b). Decoupling Path I consists of an I-shaped strip and two grounded vias. In the equivalent circuit, C_1 connects ports 1 and 2, representing the capacitive coupling

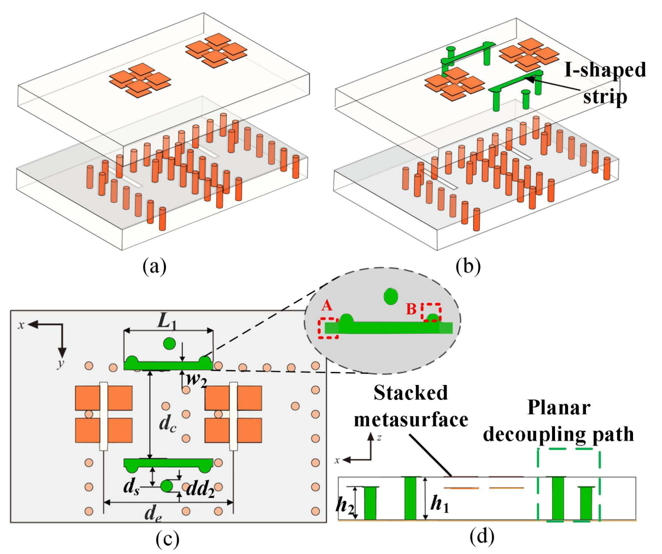

Fig. 4. Configuration of the two-elements array. (a) Without decoupling path. (b) With decoupling path. (c) Top view. (d) Side view (parameters: L_1 = 1.1 mm, W_2 = 0.1 mm, d_c = 1.2 mm, d_s = 0.35 mm, d_e = 1.6 mm, dd_2 = 0.15 mm, h_1 = 0.376 mm, and h_2 = 0.282 mm).

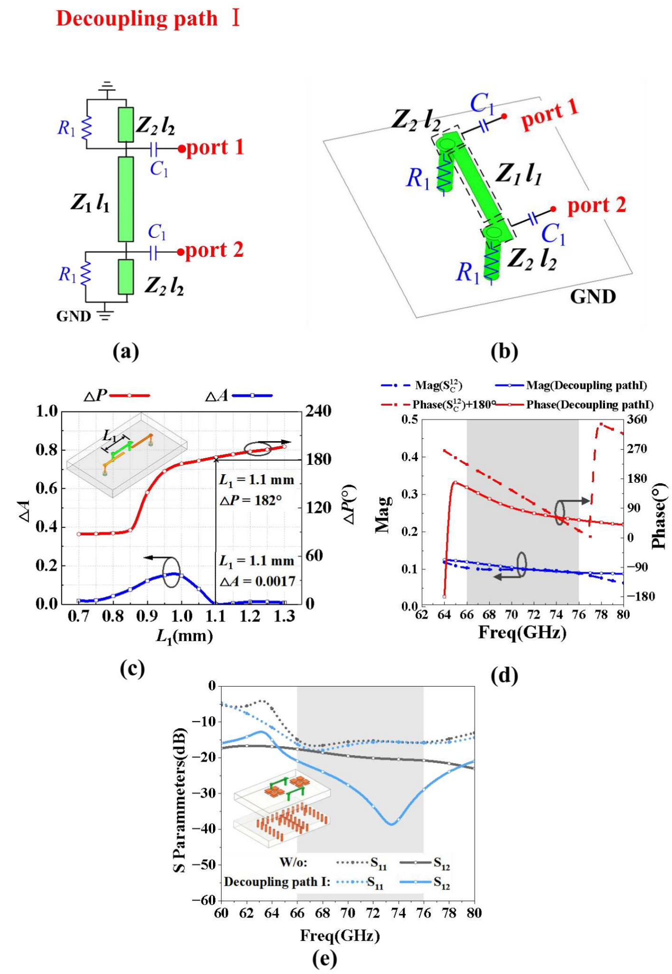

Fig. 5. Performance of Decoupling Path I. (a) Equivalent circuit, (b) HFSS simulation model, (c) amplitude difference ΔA and phase difference ΔP between S_{21}^C and S_{21}^D under different L1, (d) magnitude and phase comparison between Decoupling Path I and S_{21}^C, and (e) S-parameters of 1 × 2 array without decoupling path and with Decoupling Path I.

between the antenna and Decoupling Path I. The two grounded vias at a large height ($0.09\lambda_0$) will introduce some radiation [28], resulting in a radiation resistance R_1. Additionally, the strip near the grounded vias is denoted as Z_2. According to transmission line theory, the central connecting strip length L_1 effectively controls the phase characteristics of the Decoupling Path I by altering the equivalent electrical length of the signal transmission path. Fig. 5(c) validates this theoretical analysis: the phase difference ΔP increases gradually with L_1, whereas the amplitude difference ΔA first rises then decreases. Notably, at L_1 = 1.1 mm, ΔA approaches zero and ΔP approaches 180°. Using this optimized L_1 value in Decoupling Path I, the resulting response is compared with the inherent coupling S_{21}^C. The amplitude and phase of S_{21}^C are obtained from the two-element array without any decoupling path. As shown in Fig. 5(d), the amplitude of Decoupling Path I matches well with that of the inherent coupling S_{21}^C, but discrepancies persist in the frequency-dependent phase slope characteristics. Fig. 5(e) further demonstrates that the two-element array with the Decoupling Path I has almost no effect on its impedance matching, while achieve port isolation below −20 dB within the operational band. These experimental results confirm the effectiveness of Decoupling Path I in enhancing isolation, but the regulation of its phase slope still needs to be further optimized to achieve a more ideal decoupling effect.

To achieve enhanced phase control of the decoupling path for equal amplitude and inverse phase cancellation against inherent coupling, Decoupling Path II is realized by adding a parasitic grounded via to Decoupling Path I. Its equivalent circuit and HFSS simulation model are shown in Fig. 6(a) and (b), where the weak radiation from the parasitic grounded via is modeled as R_2, the overlying strip corresponds to Z_3 in the circuit, and capacitor C_2 maps to the distance (ds) between the parasitic grounded via and Decoupling Path I to represent the coupling energy between the parasitic via and Decoupling Path I. It should be noted that in the equivalent circuit of Decoupling Path II, the two parallel segments of Z_{11} replace Z_1 in Decoupling Path I, while other lumped parameters remain unchanged. Similar to the analysis method of Decoupling Path I, Fig. 6(c) demonstrates that ΔA decreases initially then increases with growing d_s while ΔP exhibits a linear increase, confirming that the amplitude and phase of S_{21}^D can be further controlled by parasitic grounded via. At the optimal d_s = 0.3 mm where ΔP = 174° and ΔA = 0.018 minimize the amplitude-phase discrepancy between S_{21}^C and S_{21}^D, Fig. 6(d) reveals effective amplitude and phase matching across the operational band, along with independent tuning of S_{21}^D through parameters L_1 and d_s.

Finally, through full-wave simulation analysis in HFSS, Fig. 6(e) compares the S-parameters of the two-element array under three conditions: without decoupling path, with Decoupling Path I, and with Decoupling Path II. It can be seen that the two-element array with Decoupling Path II achieves superior isolation performance, with isolation better than −25 dB and

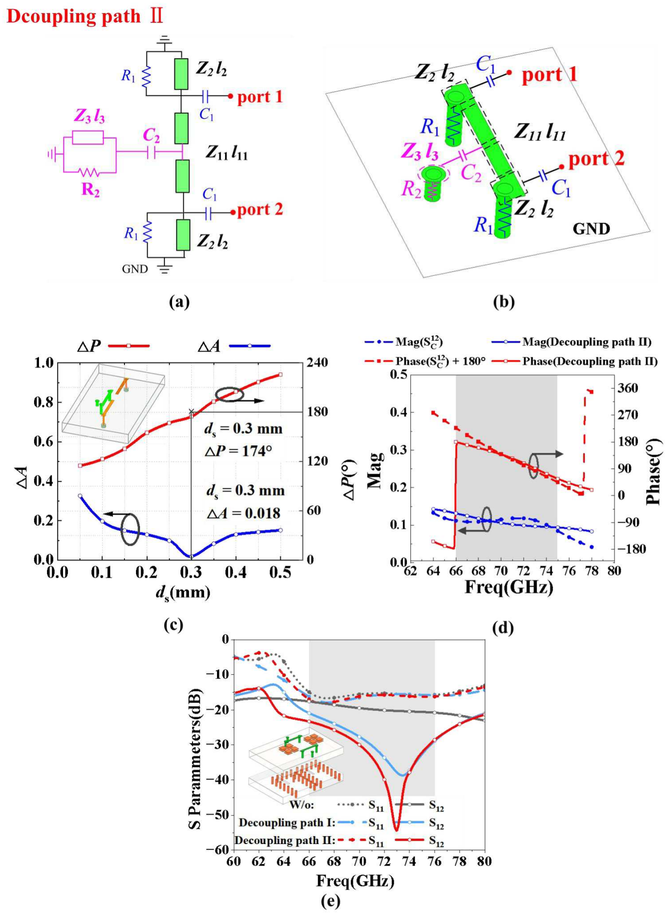

Fig. 6. Performance of Decoupling Path II. (a) Equivalent circuit, (b) physical model, (c) amplitude difference ΔA and phase difference ΔP between S_{21}^{C} and S_{21}^{D} under different ds, (d) magnitude and phase comparison between Decoupling Path II and S_{21}^{C}, and (e) S-parameters of 1×2 array without decoupling path and with Decoupling Path II.

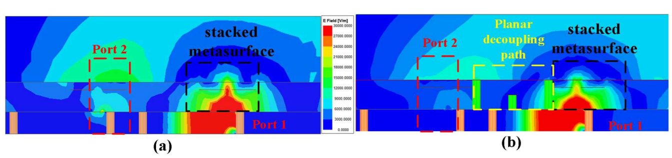

Fig. 7. Electrical field distribution of the antenna substrate. (a) Without decoupling path and (b) with decoupling path.

a minimum value reaching −55 dB. It is noteworthy that the introduction of both Decoupling Paths I and II induces negligible degradation in impedance matching characteristics, confirming that the proposed Decoupling Paths II can significantly enhance isolation while maintaining excellent impedance matching.

Subsequently, the parameters of the decoupling path are further optimized using the full-wave simulation software HFSS. The electric fields distribution of the two-elements array without and with the decoupling path is shown in Fig. 7. When port 1 is excited, the controllable decoupling path operates and the electric field at port 2 is significantly weakened. In summary, the control of amplitude and phase of the energy in the decoupling path can be realized by adjusting

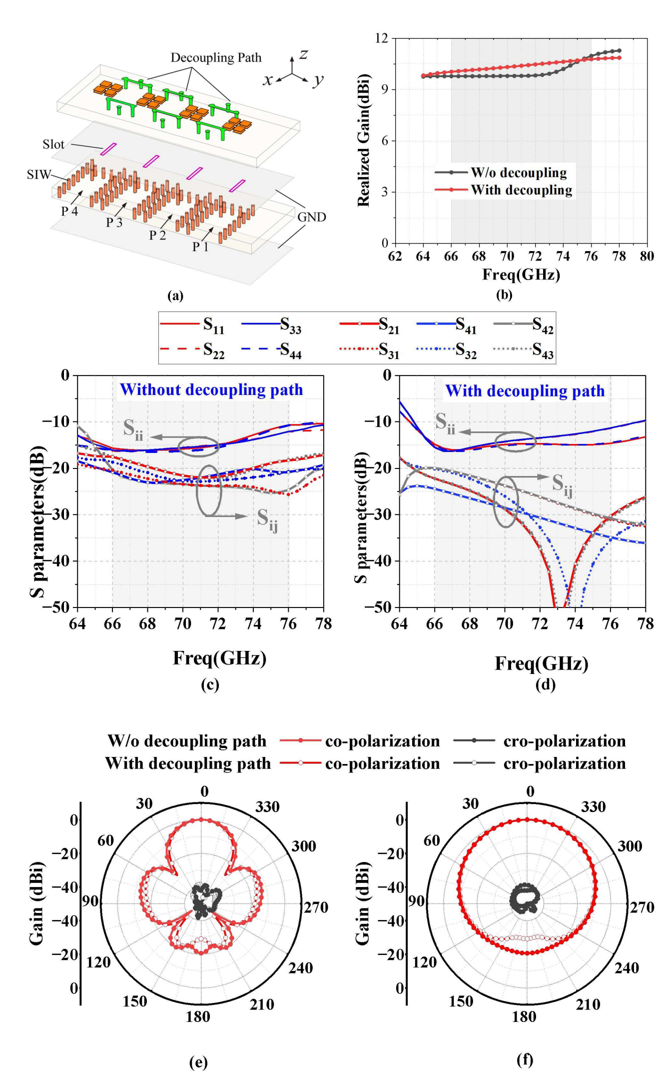

Fig. 8. Configuration and performance of 1×4 array. (a) Three-dimensional view. (b) Realized gain. (c) and (d) Comparation of S-parameters without and with decoupling paths. (e) Normalized radiation pattern of E-plane at 71 GHz. (f) Normalized radiation pattern of H-plane at 71 GHz.

d_s and L_1, and the Decoupling Path II can improve the isolation from 16.5 to 24 dB in the impedance matching bandwidth range from 66 to 76 GHz (19.6%), showing a good decoupling effect.

Then, 1×4 array is further designed to verify the performance of the proposed controllable decoupling path for large-scale array in Fig. 8(a). The decoupling paths are symmetrically positioned between the elements. Taking the middle element's port 2 as an example, the S-parameters of other ports are shown in Fig. 8(c) and (d). The isolations of adjacent ports are increased from 17 to 20 dB with minimal impact on the impedance matching of the array through the decoupling paths. As shown in Fig. 8(e) and (f), the array presents a fully coincident pattern with cross polarization suppression of more than 31 dB and gain increased by 0.7 dBi, as displayed in Fig. 8(b). The results show that the proposed controllable decoupling path exhibits good decoupling effect in 1×4 array and is expected to be applied in large-scale array.

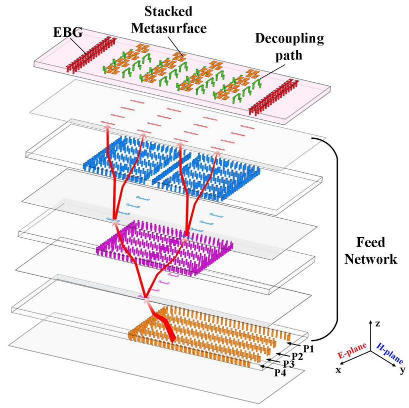

Fig. 9. Configure of 4 × 4 array loaded EBG structures.

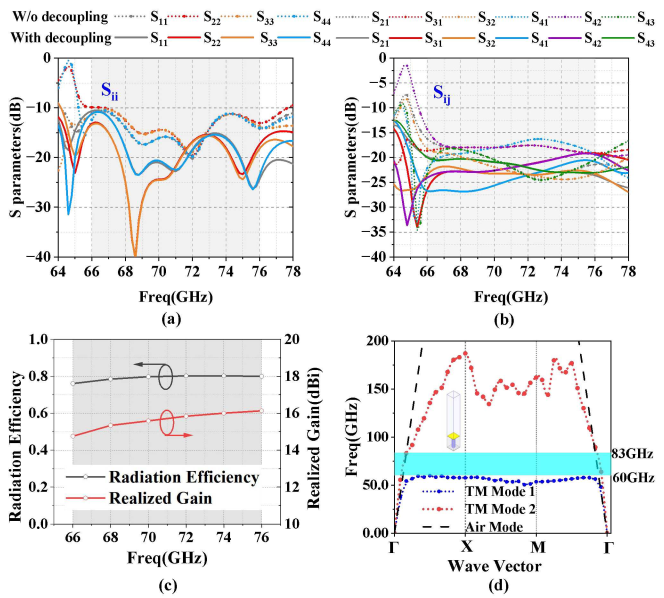

Fig. 10. S-parameters of the phased array. (a) Comparison of reflection parameters Sii without and with decoupling paths. (b) Comparison of isolation S_{ij} without and with decoupling paths. (c) Simulation gain and radiation efficiency. (d) Dispersion curve of EBG structure.

C. 4 × 4 Phased Array With EBG for Wide-Angle Scanning

In order to further verify the feasibility of the proposed controllable decoupling path in realizing a wide-angle scanning phased array, a 4 × 4 phased array antenna was designed, as depicted in Fig. 9. The phased array is comprised of the radiation elements and feeding network. The four antenna elements placed along the E-plane are treated as a subarray with a spacing of 0.38 λ_0, and controllable decoupling paths are inserted between the adjacent elements. Subarrays are then placed at a distance of 0.61 λ_0 along the H-plane. It should be noted that the distance between the H-plane subarrays is significant enough to neglect the coupling within the components. The phased array is excited by the feed network composed of bottom multilayer substrate integrated waveguide (SIW) merged through the slots. The signal passed through the T-shaped two-way power divider twice in the three-layer structure and finally achieve four-way power divider.

Moreover, in order to reduce the surface wave propagation and increase the scanning gain of the phased array, the periodic EBG structures are loaded on both sides of the antenna. The bandgap characteristic of an EBG structure is that TM waves are supported below the resonant frequency and TE waves above it. Near the resonant frequency, no waves are allowed to pass, which effectively suppress the surface waves, expand the antenna radiation to both sides, and compensate for the reduction of gain during scanning [12], [13].

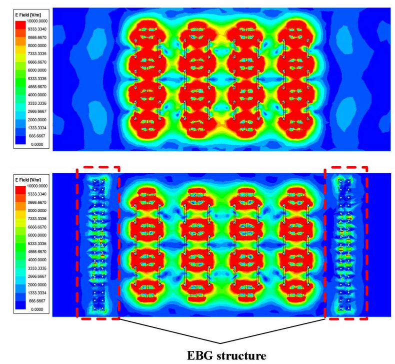

Fig. 11. Electric field of the phased array with and without EBG structures.

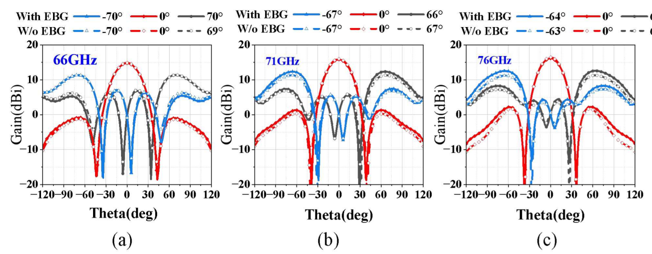

Fig. 12. Comparison of scanning performance of different frequency points after loading EBG structures. (a) 66, (b) 71, and (c) 76 GHz.

In Fig. 10(a) and (b), the S-parameters with and without decoupling path are compared. It is observed that the isolation S_{ij} between ports is increased be about 7 dB with minimal influence on impedance matching S_{ii}, and the gain remains above 15 dBi in the whole operating band, with an efficiency exceeding 71%. Moreover, as shown in Fig. 10(d), the EBG was analyzed using Floquet-port analysis, which has high impedance from 60 to 83 GHz, including the working frequency band. As shown in Figs. 11 and 12, the electric fields on both sides of the antenna array are significantly enhanced after the EBG structures are integrated. In the operating frequency band, the scanning angle is greater than 62°, and the gains of scanning are compensated about 4 dBi in the mid–high-frequency band, with a gain drop of 2.9 dBi.

As we know, the active S_m represents the energy received by *port m* from all the ports when four ports are excited by the input signals with different amplitudes and phases. It changes simultaneously with variations in the amplitude and phase of all the input signals. The relationship between the passive S-parameter S_{mn} and the active S_m given in [31] is depicted in the following equation, where $\dot{a}_n$ represents the voltage vector of *port m*:

$$\text{active } S_m = \sum_{n=1}^{N} S_{mn}\frac{\dot{a}_n}{\dot{a}_m}, \quad m = 1, \ldots, N. \tag{1}$$

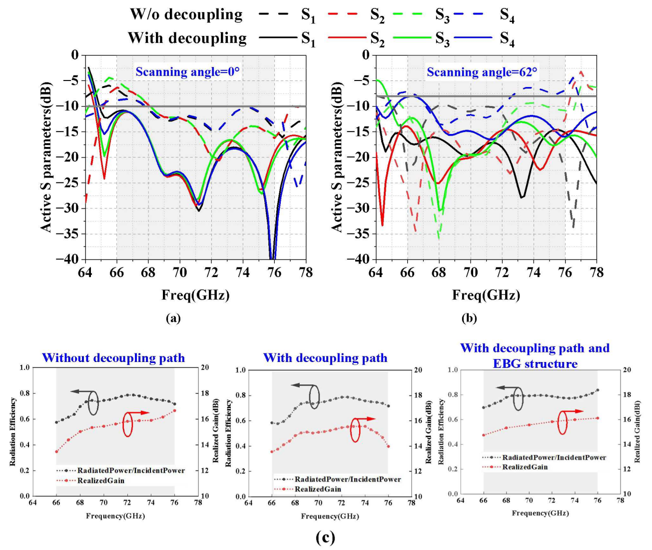

Fig. 13. Active S-parameters with and without decoupling path. (a) When scanning at 0°, (b) when scanning at 62°, and (c) total efficiency and realized gain.

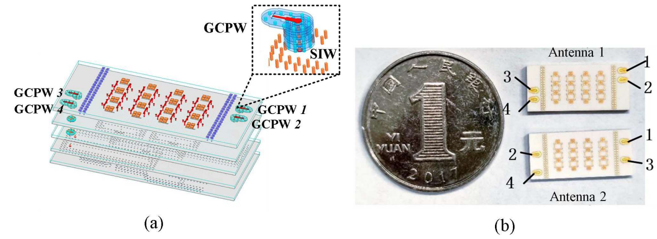

Fig. 14. Configuration of Test Antenna A. (a) Three-dimensional view. (b) Prototypes.

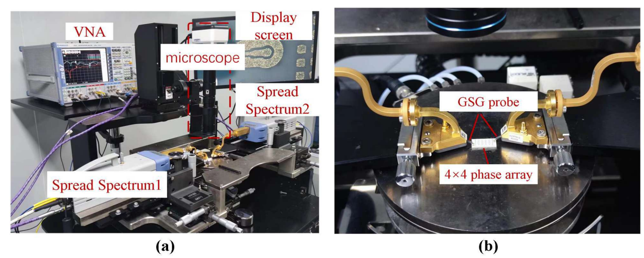

Fig. 15. Probe station S-parameter test. (a) Zoom-out view and (b) zoom-in view.

Here, the four ports of the proposed array are excited with constant amplitude and different phases, and the phase difference is determined by the desired beam angle. Equation (1) highlights that high isolation S_{mn} ensures that the active S_m remains as low as possible. As depicted in Fig. 13, within the operational band, the active S_m remains below −10 dB when no scanning, achieving a reduction of approximately 10 dB when comparing to the situation without decoupling paths, during maximum angle scanning, the active Sm remains below −8 dB, which is approximately 7 dB lower. The results show that the active S_m is reduced by the incorporation of the decoupling paths, and the radiation efficiency and gain of the wide-angle scanning array are correspondingly improved.

III. Measurements and Results

To validate the effectiveness of the proposed wide-angle scanning phased array, LTCC technology was used to fabricate the prototype. For the higher frequency range of millimeter wave, the S-parameters of the phased array were tested using a probe station, and a broadband beam-forming network was designed to verify the scanning capability of the phased array. However, there is currently no supporting phase-shifting equipment available to test the scanning performance of the array. Therefore, this section presents the design of three test antennas to evaluate the performance of the mm-Wave phased array.

1) Test Antenna A is used to test the S-parameters of the phased array, including the return loss and the isolation.
2) Test Antenna B is used to measure the gain and radiation pattern of the array when it is no-scanning.
3) Test Antenna C is used to evaluate the scanning performance of the array, when applying signals with a phase difference of −150° and +150° between adjacent four ports.

A. S-Parameters and Isolation Measurement of the Fabricated Array A Using Probe Table

According to the requirements of machining and testing of the array's S-parameters, the GSG test structure for mm-Wave probe testing has been incorporated onto the upper surface of the previously designed phased array. As depicted in Fig. 14, the signal is transmitted from the feeding network layer to the upper surface of the phased array through the SIW to GCPW transition structure. Furthermore, the impact of the GSG pad on array radiation is effectively reduced by the EBG structures of the array layers. A complete isolation test using a probe station necessitates the use of two antennas, and both antennas can conduct return loss tests on four ports. Specifically, Antenna 1 is utilized to test the isolation between $S_{12}/S_{14}/S_{32}/S_{34}$, while Antenna 2 is employed to test the isolation between ports $S_{13}/S_{14}/S_{23}/S_{24}$.

The prototypes, as shown in Fig. 14(b), have the antenna dimensions of 8.1 × 17.83 × 1.55 mm. The front side features the stacked metasurface antenna elements, controllable decoupling paths, EBG structures, and GSG test pads, while the back side is a metal ground plane. Fig. 15 depicts the controlled environment of the probe station test system. During testing, the 4 × 4 phased array under test is securely fastened onto the test fixture, while the two waveguide probes are securely linked to the fixed 50–70-GHz frequency expander on the probe station via curved waveguide transmission lines. Subsequently, these probes are connected to the vector network analyzer (VNA) using an RF transmission line, facilitating the measurement of S-parameters. Furthermore, the two probes can move independently along the *x*-, *y*-, and *z*-axes relative to the base of the probe station module, ensuring precise and dependable contact between the probe and the antenna being measured. It is worth noting that the probe utilized in the probe station test system for mm-Wave application is the ACP GSG waveguide probe.

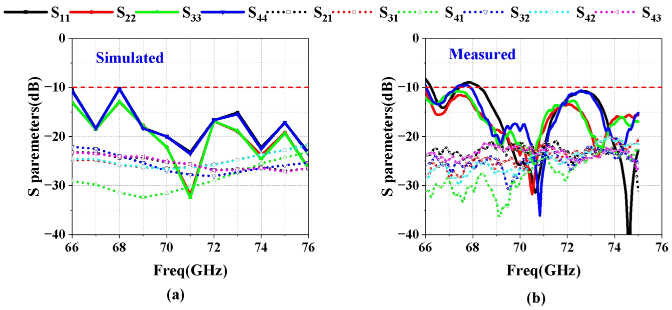

Fig. 16. (a) Simulated and (b) measured of S-parameters.

TABLE I
SIMULATION AND MEASURED PERFORMANCE OF TEST ANTENNA A

Test Antenna A		S_{ii} (66-76 GHz)	Isolation
	simulated	-10 dB	22 dB
	measured	-8 dB	20 dB

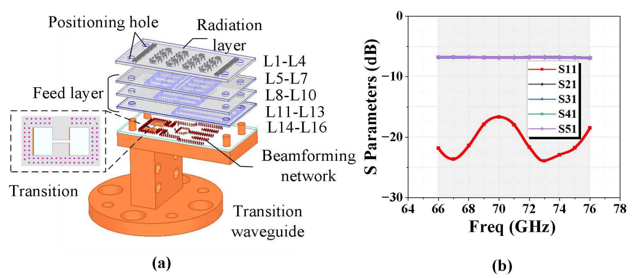

Fig. 17. Configuration of Test Antenna B with beamforming network. (a) Three-dimensional view. (b) S-parameters of transition from SIW to waveguide.

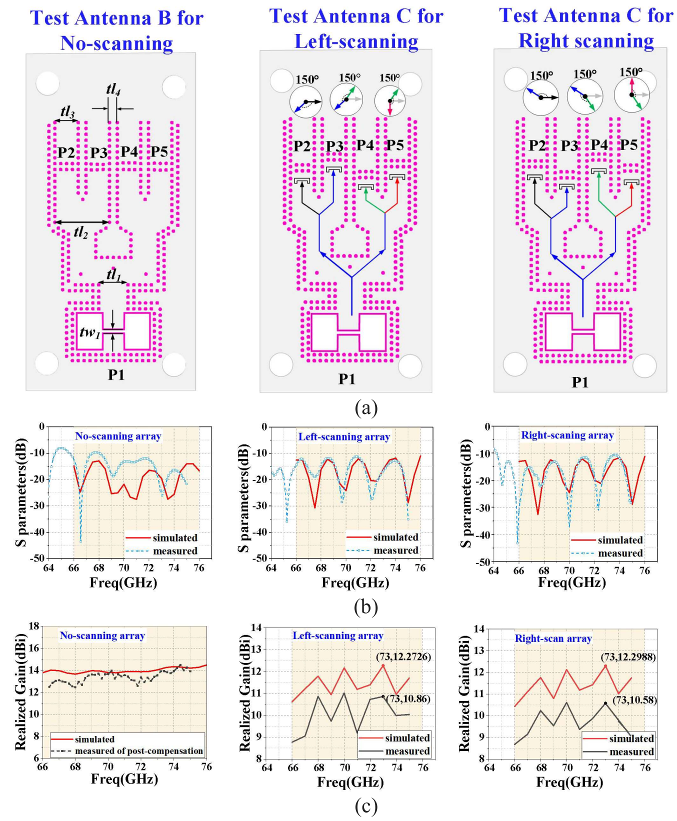

Fig. 18. Beamforming network and performance of three test antennas. (a) Beamforming network, (b) reflection coefficients, and (c) realized gain (parameters: tw1 = 0.2 mm, tl1 = 1.1 mm, tl2 = 2.8 mm, tl3 = 1.2 mm, tl4 = 0.6 mm, and tl5 = 0.4 mm).

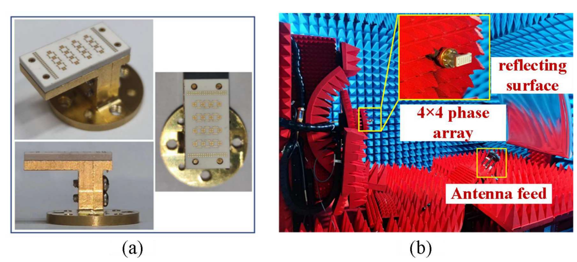

Fig. 19. Physical picture of Test Antennas B and C. (a) Physical samples. (b) Test environment.

Fig. 16 and Table I present a comparison of S-parameters simulated and measured results. The results show that the S-parameters of the antenna test can be matched in the range of 66–76 GHz, and the in-band impedance matching is less than −8 dB. The difference of the results can be attributed to the variance between the port setting mode in the antenna simulation and the microwave probe in the actual measurement. Second, as the frequency increases, the probe has weak radiation characteristics, which will inevitably cause interference to the test antenna.

B. Beam Scanning Measurement of the Fabricated Array B With SIW Beam-Forming Network

Test Antenna B can be utilized to evaluate the radiation gain and radiation pattern when the phased array is not being scanned. As illustrated in Fig. 17, Test Antenna B is composed of L1–L4 as the radiation layer, L5–L13 as a multilayer 1:4 feed network, and L14–L16 as a planar 1:4 beamforming network composed of SIW. The WR15 rectangular waveguide is used to feed Test Antenna B, and the double-ridged rectangular transition from SIW to waveguide is vertically located under the SIW four-way power divider and used to improve their impedance mismatching. Then, the transition is finally connected with WR15 rectangular waveguide with standard flanges. In addition, to ensure precise positioning of the waveguide port during the welding process, two positioning holes are incorporated on each side of the antenna. The S-parameters with transition structure are shown in Fig. 17(b). The average loss when $S_{11} < -15$ dB is about 0.85 dB within working frequency band.

In order to evaluate the scanning performance of the phased array, Test Antenna C was designed on the basis of Test Antenna B, and a beamforming network composed of SIW was loaded under the antenna feeding network. Beamforming network includes four-way power divide with constant amplitude and phase at no-scan and beamforming network at left and right-scanning. It is composed by a 1:4 power division network fed by a waveguide and a U-shaped slot with relative path difference. As shown in Fig. 18(a), the required phase shift is achieved by controlling the path difference of the four U-

TABLE II
SIMULATION AND MEASURED PERFORMANCE OF TEST ANTENNAS B AND C

Test antenna		Return Loss	Gain	Beam direction
B (No-scanning)	Simulated	-13 dB	13.7-14.3 dBi	0°
	measured	-10 dB	12.5-14.5 dBi	0°
C (Left-scanning)	Simulated	-12 dB	10.6-12.3 dBi	-69° ~ 61°
	measured	-11.3 dB	8.8-11 dBi	-68° ~ 62°
C (Right-scanning)	Simulated	-11.7 dB	10.4-12.3 dBi	62° ~ 69°
	measured	-10.7 dB	8.7-10.6 dBi	62° ~ 68

TABLE III
COMPARISON WITH OTHER mm-WAVE PHASE ARRAYS

Ref.	**Decoupling method**	**Scale**	**Element space**	**Bandwidth**	**Act.S/ Isolation**	**Scanning angle**	**Gain drop**
Pattern reconfigurable stacked patch antenna [27]	Shorted rectangular loop	4×4	$0.98\lambda_0$	9.7% (24.5-27GHz)	N.A./⩾17dB	±55°	< 4.2dB
Patch array with decoupling structures[28]	Planar decoupling path	4×4	$0.45\lambda_0$	16.7% (25-29.5GHz)	<-10dB/⩾22dB	±50°	< 4dB
L-shaped probe-fed phased array antenna (AiP) [29]	N.A	4×4	$0.6\lambda_0$	23.2% （51-64GHz）	N.A./⩾20dB	±30°	<3.5dB
Wideband integrated array antenna [30]	N.A	16×16	$0.93\lambda_0$	10.5% (71-76GHz)	N.A./≥20dB	N.A	< 2.5dB
This Work	**Controllable planar decoupling path**	**4×4**	$\mathbf{0.38\lambda_0}$	**19.7% (66-76GHz)**	**<-10dB /⩾20dB**	**> ±62° (in the whole band)**	**< 2.9dB (at all scanning angles)**

slot couplers to generate a phase difference between adjacent channels. When no-scanning, the phase difference between the ports is 0. When scanning, the different phase difference between the adjacent ports can realize the left and right scanning of the phased array. For left-scanning at 71 GHz, the phase difference between P2 and P3 ports is −146°, the P3 and P4 ports is −157°, and the P4 and P5 is −148°. Right-scanning beamforming network is inherently symmetric to left-scanning beamforming network, so I would not delve into the details here.

Fig. 19(a) shows a physical sample of Test Antennas B and C, with dimensions of 8.7 × 17.83 × 1.55 mm. The front of the antenna is composed of stacked metasurface antenna elements, controllable decoupling path, EBG structures, and positioning holes, and the white H-shaped structure on the back is the waveguide transition port of the phased array. The radiation characteristics of the 4 × 4 phased array were tested in a close-field darkroom, and the test environment was shown in Fig. 19(b). As shown in Fig. 18(b), the simulation and measured results of the S-parameters of the no-scan, left-scan, and right-scan antennas are, respectively, compared. It can be seen that the resonant frequency points measured by antenna S-parameters are basically consistent with the simulated resonant frequency points, and the impedance matching is less than −10 dB. Fig. 18(c) shows the array gain measured in the near-field chamber. The results show that the measured gain is over 12 dBi, and the frequency gain curve of the left and right scanning maximum beam direction is consistent with the simulation trend, with a drop of about 1.5 dBi. Finally, the simulated and measured performance of antenna scanning at three different frequencies are analyzed. The detailed results are shown in Fig. 20. In the range of 66–76 GHz, the scan range is 62°–68°, and in the wide-angle scanning, the gain drop remains below or around −2.9 dBi. Compared with the simulated results, the scanning range of the measured is slightly narrower, which may be due to the imperfect measurement operation. The simulated and measured results of Test Antennas B and C are summarized in Table II.

C. Performance Comparison

For demonstration, comparisons with other previously reported mm-Wave beam-scanning phased array are also concluded in Table III. The studies in [27] and [28], operating in the Ka-band, employ decoupling structures to enhance isolation but exhibit relatively limited operating bandwidth and scanning range. Similarly, the devices in [29] and [30], operating in the E-band, achieve a high isolation level of 20 dB, but with a relatively narrow scanning range. These works highlight the challenges in achieving a balanced performance in bandwidth, scanning range, and isolation at mm-Wave frequencies. In contrast, the proposed design attains a high isolation of 20 dB over a wide operating bandwidth of 19.7%, an active S-parameters remain below –10 dB, and a scanning range exceeding ±62°. The results demonstrate that the antenna array using controllable decoupling paths

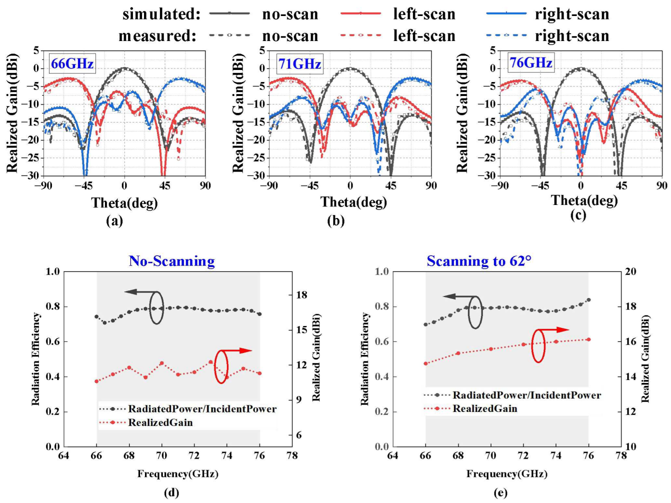

Fig. 20. Simulated and measured results of antenna radiation pattern at three different frequencies. (a) 66, (b) 71, and (c) 76 GHz. (d) Total efficiency and realized gain when no-scanning. (e) Total efficiency and realized gain when no-scanning.

effectively enhances the overall performance for wideband and wide-angle scanning while maintaining a compact array configuration.

IV. Conclusion

In this work, a new decoupling path is proposed, which achieves constant amplitude and inverse phase decoupling alongside the inherent coupling, effectively eliminating the inherent coupling without altering the antenna radiation. Through this method, a high isolation of 20 dB at a wideband of 19.7% can be achieved by the mm-Wave phased array prototype, while active S-parameters are maintained below −10 dB. Consequently, the phased array antenna loaded with the controllable decoupling paths offers the benefits of high isolation and good active S-parameters, presenting promising applications in mm-Wave communication systems.

References

[1] D. Liu, U. Pfeiffer, J. Grzyb, and B. Gaucher, *Advanced Millimeter-Wave Technologies: Antennas, Packaging and Circuits*. Hoboken, NJ, USA: Wiley, 2009.

[2] J. Hirokawa, "Millimeter-wave antenna technologies for 5G mobile communication systems," in *Proc. IEEE Int. Workshop Electromagn., Appl. Student Innov. Competition (iWEM)*, May 2016, pp. 1–3.

[3] X. Ding, Y.-F. Cheng, W. Shao, and B.-Z. Wang, "A wide-angle scanning phased array with microstrip patch mode reconfiguration technique," *IEEE Trans. Antennas Propag.*, vol. 65, no. 9, pp. 4548–4555, Sep. 2017.

[4] Y.-Y. Bai, S. Xiao, M.-C. Tang, Z.-F. Ding, and B.-Z. Wang, "Wide-angle scanning phased array with pattern reconfigurable elements," *IEEE Trans. Antennas Propag.*, vol. 59, no. 11, pp. 4071–4076, Nov. 2011.

[5] G. Federico, G. Theis, D. Caratelli, and A. B. Smolders, "Extending the scan range of phased arrays using reconfigurable antenna elements," in *Proc. 17th Eur. Conf. Antennas Propag. (EuCAP)*, Florence, Italy, Mar. 2023, pp. 1–4.

[6] A. G. Toshev, "Multipanel concept for wide-angle scanning of phased array antennas," *IEEE Trans. Antennas Propag.*, vol. 56, no. 10, pp. 3330–3333, Oct. 2008.

[7] B. Nie et al., "Fully metallic gradient index lens array antenna for wide-angle scanning phased array," *IEEE Trans. Antennas Propag.*, vol. 71, no. 9, pp. 7363–7375, Sep. 2023.

[8] J. G. Marin and J. Hesselbarth, "Lens antenna with planar focal surface for wide-angle beam-steering application," *IEEE Trans. Antennas Propag.*, vol. 67, no. 4, pp. 2757–2762, Apr. 2019.

[9] A. Foroozesh and L. Shafai, "Investigation into the application of artificial magnetic conductors to bandwidth broadening, gain enhancement and beam shaping of low profile and conventional monopole antennas," *IEEE Trans. Antennas Propag.*, vol. 59, no. 1, pp. 4–20, Jan. 2011.

[10] Z. N. Chen, W. Liu, and X. Qing, "Low-profile broadband mushroom and metasurface antennas," in *Proc. Int. Workshop Antenna Technol., Small Antennas, Innov. Struct., Appl. (iWAT)*, Athens, Greece, Mar. 2017, pp. 13–16.

[11] Nasimuddin and X. Qing, "A miniaturized wideband circularly polarized antenna using metasurface," in *Proc. 16th Eur. Conf. Antennas Propag. (EuCAP)*, Madrid, Spain, Mar. 2022, pp. 1–5.

[12] L. Zhao, Y. He, G. Zhao, X. Chen, G.-L. Huang, and W. Lin, "Scanning angle extension of a millimeter-wave antenna array using electromagnetic band gap ground," *IEEE Trans. Antennas Propag.*, vol. 70, no. 8, pp. 7264–7269, Aug. 2022.

[13] D. Sievenpiper, L. Zhang, R. F. J. Broas, N. G. Alexopolous, and E. Yablonovitch, "High-impedance electromagnetic surfaces with a forbidden frequency band," *IEEE Trans. Microw. Theory Techn.*, vol. 47, no. 11, pp. 2059–2074, Nov. 1999.

[14] L. Zhu, H. Jin, X. Liu, and G. Yang, "Wide-angle scanning phased array based on a microstrip magnetic dipole for K band radar systems," in *Proc. IEEE Int. Symp. Antennas Propag. USNC/URSI Nat. Radio Sci. Meeting*, Boston, MA, USA, Jul. 2018, pp. 1853–1854.

[15] G. Yang, Q. Chen, J. Li, S. Zhou, and Z. Xing, "Improving wide-angle scanning performance of phased array antenna by dielectric sheet," *IEEE Access*, vol. 7, pp. 71897–71906, 2019.

[16] X. Yang, Y. Liu, Y.-X. Xu, and S.-x. Gong, "Isolation enhancement in patch antenna array with fractal UC-EBG structure and cross slot," *IEEE Antennas Wireless Propag. Lett.*, vol. 16, pp. 2175–2178, 2017.

[17] C. Zhou, W. Yang, Q. Xue, Y. Liu, Y. Xu, and W. Che, "Millimeter-wave wideband dual-polarized LTCC antenna array based on metasurfaces for beam-scanning applications," *IEEE Trans. Antennas Propag.*, vol. 70, no. 10, pp. 9912–9917, Oct. 2022.

[18] N. Zhou and S. Zheng, "A low-profile wideband wide-angle scanning tightly coupled dipole array antenna," in *IEEE MTT-S Int. Microw. Symp. Dig.*, Nanjing, China, May 2021, pp. 1–3.

[19] F. Yang and Y. Rahmat-Samii, "Microstrip antennas integrated with electromagnetic band-gap (EBG) structures: A low mutual coupling design for array applications," *IEEE Trans. Antennas Propag.*, vol. 51, no. 10, pp. 2936–2946, Oct. 2003.

[20] Z. Wang, C. Li, Q. Wu, and Y. Yin, "A metasurface-based low-profile array decoupling technology to enhance isolation in MIMO antenna systems," *IEEE Access*, vol. 8, pp. 125565–125575, 2020.

[21] D. Chen, W. Yang, S. Pan, Q. Xue, and W. Che, "Millimeter-wave 45∘-polarized LTCC phased array using wide-beam patch-via-wall elements for wide-angle scanning applications," *IEEE Trans. Antennas Propag.*, vol. 71, no. 12, pp. 9497–9508, Dec. 2023.

[22] R.-L. Xia, S.-W. Qu, P.-F. Li, D.-Q. Yang, S. Yang, and Z.-P. Nie, "Wide-angle scanning phased array using an efficient decoupling network," *IEEE Trans. Antennas Propag.*, vol. 63, no. 11, pp. 5161–5165, Nov. 2015.

[23] P. Mei, Y.-M. Zhang, and S. Zhang, "Decoupling of a wideband dual-polarized large-scale antenna array with dielectric stubs," *IEEE Trans. Veh. Technol.*, vol. 70, no. 8, pp. 7363–7374, Aug. 2021.

[24] Y. Li and Q.-X. Chu, "Dual-layer superstrate structure for decoupling of dual-polarized antenna arrays," *IEEE Antennas Wireless Propag. Lett.*, vol. 21, no. 3, pp. 521–525, Mar. 2022.

[25] W. Yang, L. Chen, S. Pan, W. Che, and Q. Xue, "Novel decoupling method based on coupling energy cancellation and its application in 5G dual-polarized high-isolation antenna array," *IEEE Trans. Antennas Propag.*, vol. 70, no. 4, pp. 2686–2697, Apr. 2022.

[26] Y.-M. Zhang, X. Li, and S.-Q. Xiao, "A simple decoupling method for millimeter-wave aperture-coupled patch antenna arrays," in *Proc. Int. Workshop Antenna Technol. (iWAT)*, Aalborg, Denmark, May 2023, pp. 1–3.

[27] Z. Ding, J. Chen, H. Zhou, and R. Jin, "Two-dimensional scanning phased array with large element spacing using pattern reconfigurable stacked patch antenna at Ka-band," *IEEE Trans. Antennas Propag.*, vol. 70, no. 7, pp. 5447–5457, Jul. 2022.

[28] L. Gu, W. Yang, S. Liao, Q. Xue, and W. Che, "Novel coupling cancellation method by loading planar path for wideband high-isolation wide-scanning millimeter-wave phased array," *IEEE Trans. Antennas Propag.*, vol. 70, no. 11, pp. 10520–10530, Nov. 2022.

[29] H. Xia et al., "A cost-effective wideband dual-polarized L-shaped probe-fed phased array antenna for 60-GHz AiP applications," *IEEE Trans. Compon., Packag., Manuf. Technol.*, vol. 13, no. 11, pp. 1790–1803, Nov. 2023.

[30] L. Wang, Y. J. Cheng, D. Ma, and C. X. Weng, "Wideband and dual-band high-gain substrate integrated antenna array for E-band multi-gigahertz capacity wireless communication systems," *IEEE Trans. Antennas Propag.*, vol. 62, no. 9, pp. 4602–4611, Sep. 2014.

[31] M. Kalfa and E. Halavut, "A fast method for obtaining active S-parameters in large uniform phased array antennas," in *Proc. IEEE Int. Symp. Phased Array Syst. Technol.*, Waltham, MA, USA, Oct. 2013, pp. 684–688.

Wanchen Yang (Senior Member, IEEE) was born in Xuzhou, Jiangsu, China, in 1988. She received the B.Eng. degree in communication engineering from Hohai University (HHU), Nanjing, China, in 2010, and the Ph.D. degree in electromagnetic field and microwave technology from Nanjing University of Science and Technology (NUST), Nanjing, in 2015.

From November 2013 to April 2014, she was a Research Assistant with the University of Macau, Macau, China. From May 2017 to November 2017, she is a Post-Doctoral Fellow with the City University of Hong Kong, Hong Kong. She served as an Assistant Professor at NUST, from 2015 to 2018; then as an Associate Professor at South China University of Technology, from 2019 to 2022, and subsequently as a Professor at Hohai University, from 2022 to 2024. In August 2024, she joined Nanjing University of Aeronautics and Astronautics, Nanjing, where she is currently a Professor. She has authored or co-authored over 100 Journal articles including 51 in IEEE TRANSACTIONS, garnering over 4000 citations on Google Scholar and H-index of 38. Her main research interests include metasurface-based antenna arrays, multifunctional antenna arrays, millimeter-wave phased arrays in package, and MIMO antenna arrays and technologies.

Dr. Yang is a Technical Committee Member of IEEE APS Technical Committee on Antenna Measurement (TCAM). She was a recipient of the 2017 Outstanding Doctoral Dissertation of Jiangsu Province, the 2021 Second Prize of Science and Technology Progress Award of Chinese Institute of Electronics (CIE), and the 2024 Second Prize of Natural Science Award of Chinese Institute of Communication (CIC). She has also been recognized with multiple Best Student Paper Awards as an Advisor or a Co-Advisor at international conferences, including APMC in 2015, ICMMT in 2016, GSMM in 2017, IEEE IWS in 2022 and 2023, IEEE ICCEM in 2024, and IEEE iWEM in 2025, among others. She serves as an Area Editor for the *Microwave and Optical Technology Letters* and an Associate Editor for IEEE ACCESS, and a reviewer for IEEE TRANSACTIONS ON ANTENNAS AND PROPAGATION, IEEE TRANSACTIONS ON MICROWAVE THEORY AND TECHNIQUES, IEEE TRANSACTIONS ON INDUSTRIAL ELECTRONICS, and IEEE ANTENNAS AND WIRELESS PROPAGATION LETTERS.

Zhixin Liang was born in Yunnan, China, in 2003. She received the B.Eng. degree from College of Information Science and Engineering, Hohai University (HHU), Nanjing, China, in 2025.

Her current research interests include metasurface antennas and wide-angle scanning phased arrays.

Xiangchuan Wang (Member, IEEE) received the B.Eng. degree in automation and the Ph.D. degree in microelectronics and solid-state electronics from Nanjing University, Nanjing, China, in 2009 and 2015, respectively.

He is currently a Professor with the National Key Laboratory of Microwave Photonics, Nanjing University of Aeronautics and Astronautics, Nanjing. He has authored or co-authored over 90 research papers. His current research interests include microwave photonic measurement and synchronization, distributed microwave photonic radar, and microwave photonic imaging radar.

Xufu Liu was born in Guangdong, China, in 1998. He received the B.S. degree in electronic and information engineering from Jinan University, Guangzhou, China, in 2020, and the M.S. degree in information and communication engineering from South China University of Technology, Guangzhou, in 2023.

His current research interests include metasurface antennas, radar transceiver antennas, and wide-angle scanning phased arrays.

Wenjie Feng (Senior Member, IEEE) was born in Shangqiu, Henan, China, in 1985. He received the B.Sc. degree from the First Aeronautic College of the Airforce, Xinyang, China, in 2008, and the M.Sc. and Ph.D. degrees from Nanjing University of Science and Technology (NUST), Nanjing, China, in 2010 and 2013, respectively.

From July 2017 to September 2017, he was a Research Fellow with the City University of Hong Kong, Hong Kong. From October 2010 to March 2011, he was an Exchange Student with the Institute of High Frequency Engineering, Technische Universität München, Munich, Germany. He is currently a Professor with South China University of Technology, Guangzhou, China. He has authored or co-authored over 140 IEEE journal articles (including 100 IEEE TRANSACTIONS article) and 100 conference papers. His research interests include wideband circuits and technologies, microwave and millimeter-wave circuits and components, circuits interconnection, and packaging.

Dr. Feng was a recipient of the National Science Fund for Excellent Young Scholars in 2018, the Young Scientist Award of ACES-China, and a reviewer for over 20 Internationally Refereed Journals and Conferences. He currently serves as an Associate Editor for *IET Microwaves, Antennas and Propagation*, *IET Electronics Letters*, and *International Journal of Electronics*.

Wenquan Che (Fellow, IEEE) received the B.Sc. degree from East China Institute of Science and Technology, Nanjing, China, in 1990, the M.Sc. degree from Nanjing University of Science and Technology (NUST), Nanjing, in 1995, and the Ph.D. degree from the City University of Hong Kong, Hong Kong, in 2003.

In 1999, she joined the City University of Hong Kong, as a Research Assistant, where she was a Research Fellow and a Visiting Professor, from 2005 to 2006 and 2009 to 2011. In 2002, she joined Polytechnique Montréal, Montreal, QC, Canada, as a Visiting Scholar. From 2007 to 2008, she was with the Institute of High Frequency Technology, Technische Universität München, Munich, Germany. From 2008 to October 2018, she was a Professor with Nanjing University of Science and Technology. In November 2018, she joined South China University of Technology, Guangzhou, China, where she is currently a Professor. She has authored or co-authored over 300 internationally refereed journal articles and international conference papers. Her research interests include electromagnetic computation, planar/coplanar circuits and subsystems in RF/microwave frequency, microwave monolithic integrated circuits (MMICs), and medical application of microwave technology.

Dr. Che is a member of IEEE MTT-S AdCom Committee from 2018 to 2020. She was a recipient of the 2007 Humboldt Research Fellowship presented by the Alexander von Humboldt Foundation of Germany, the 5th China Young Female Scientists Award in 2008, and the Distinguished Young Scientist awarded by the National Natural Science Foundation Committee (NSFC) of China in 2012. She is the Editor-in-Chief for the *Microwave and Optical Technology Letters*, an Associate Editor of IEEE JOURNAL OF ELECTROMAGNETICS, RF AND MICROWAVES IN MEDICINE AND BIOLOGY, and a reviewer of IEEE TRANSACTIONS ON MICROWAVE THEORY AND TECHNIQUES, IEEE TRANSACTIONS ON ANTENNAS AND PROPAGATION, IEEE TRANSACTIONS ON INDUSTRIAL ELECTRONICS, and IEEE MICROWAVE AND WIRELESS COMPONENTS LETTERS.

Shilong Pan (Fellow, IEEE) received the B.S. and Ph.D. degrees in electronic engineering from Tsinghua University, Beijing, China, in 2004 and 2008, respectively.

From 2008 to 2010, he was a "Vision 2010" Post-Doctoral Research Fellow at the Microwave Photonics Research Laboratory, University of Ottawa, Ottawa, ON, Canada. He joined Nanjing University of Aeronautics and Astronautics, Nanjing, China, in 2010, where he is currently a Full Professor and the Director of the National Key Laboratory of Microwave Photonics, Nanjing. His research has focused on microwave photonics. He has authored or co-authored over more than 350 articles in peer-reviewed journals and 300 papers in conference proceedings.

Prof. Pan is a fellow of Optica, SPIE, and IET. He was a recipient of IEEE MTT-S Outstanding Young Engineer Award in 2021. He is the Vice Chair of IEEE MTT-22 Microwave Photonics. He has also served as a Chair of a number of international conferences, symposia, and workshops, including the TPC Chair of IEEE International Topical Meeting on Microwave Photonics (MWP) in 2023, a TPC Co-Chair of IEEE MWP 2017, and the General Co-Chair of IEEE MWP 2021 and 2025. He was selected as an IEEE Photonics Society Distinguished Lecturer in 2019 and an IEEE MTT-S Distinguished Microwave Lecturer in 2022. He is currently a Senior Editor of *PhotoniX* and an Associate Editor of IEEE/OPTICA JOURNAL OF LIGHTWAVE TECHNOLOGY and IEEE TRANSACTIONS ON MICROWAVE THEORY AND TECHNIQUES.